Net Electronic Charge as an Effective Electronic Descriptor for Oxygen Release and Transport Properties of $SrFeO_3$-based Oxygen Sorbents

Xijun Wang, Emily Krzystowczyk, Jian Dou, Fanxing Li*

Department of Chemical and Biomolecular Engineering, North Carolina State University, 911 Partners Way, Raleigh, North Carolina 27695-7905, United States

ABSTRACT: Resulting from their excellent redox properties and high tunability, perovskite oxides, as oxygen sorbents, exhibit excellent potential in thermochemical redox applications such as chemical looping air separation (CLAS). The structural and compositional flexibility of perovskites, while making these mixed-oxides highly versatile, also poses challenges for their design and optimization. Moreover, the elevated operating temperature and dynamic oxygen partial pressure swings during redox processes add additional complications for oxygen sorbent design. From a fundamental standpoint, finding simple yet effective descriptors for the effect of cation substitutions on oxygen sorbents' redox and oxygen transport properties are of significant importance for rational optimization of perovskite-based oxygen sorbents. In the present study, a series of A/B-site doped $SrFeO_{3-\delta}$ perovskites are investigated using DFT+U simulations. From these simulations, an effective electronic structure descriptor, the net electronic charge (Δe) of oxygen anions, is extracted based on its excellent correlations with vacancy formation energy, experimentally derived oxygen capacity, and oxygen vacancy migration barrier. These findings provide an effective tool to correlate the oxygen sorbents' redox performances with a simple yet physically meaningful descriptor for rational design and optimization of perovskites in the context of CLAS.

1. INTRODUCTION

Chemical looping, as an emerging strategy for reactive oxygen separation, offers a potentially efficient and cost-effective approach for carbonaceous energy conversion, carbon dioxide capture, and chemical production.[1-4] The concept of chemical looping has been extensively studied over a wide range of applications such as chemical looping air separation (CLAS),[5,6] chemical looping partial oxidation (CLPO) of methane,[7,8] chemical looping – oxidative dehydrogenation (CL-ODH) of ethane and propane,[9-11] and redox oxidative cracking (ROC) of naphtha,[12,13] etc. The underlying principle of chemical looping is the use of an oxygen carrier, also known as an oxygen sorbent or redox catalyst, to spontaneously release and replenish lattice oxygen under oxygen partial pressure (P_{O_2}) and/or temperature swings.[14] Therefore, the oxygen carrier performances, including redox and oxygen transport properties, play a critical role in the overall efficiency of a chemical looping process. In terms of their compositions, oxygen carriers are typically composed of (supported) transition metal oxides and their combinations,[15,16] natural ores[17,18] and mixed metal oxides such as perovskite oxides.[19] Among these, perovskites show great potential due to their remarkable structural and compositional versatility, which leads to tunable redox and oxygen transport properties in the context of chemical looping.[20-22] Standard perovskite oxides have a general stoichiometry of $ABO_{3-\delta}$, where A is typically composed of alkaline earth, rare earth, and/or alkali metal cations, while B can usually be transition metals or several main group elements such as Al, Ga or Bi.[23] The substitution of A or B-site cation in perovskites was known to be an effective strategy to tailor their redox properties for chemical looping applications such as chemical looping air separation (CLAS).[23-25]

Among the various perovskite based oxygen sorbents investigated to date,[14,26-32] doped strontium ferrite ($SrFeO_{3-\delta}$, SF) family of materials exhibit excellent potential for CLAS.[5,33] A number of doped SF sorbents, such as $Sr_xLa_{1-x}FeO_{3-\delta}$,[34] $Sr_xCa_{1-x}FeO_{3-\delta}$,[35] $SrFe_yCu_{1-y}O_{3-\delta}$,[25] and $SrFe_yMn_{1-y}O_{3-\delta}$,[36] have demonstrated suitable thermodynamic properties, excellent redox stability, and significant oxygen carrying capacity at relatively low temperatures.[34] Despite these merits, the practical utilization of SF based oxygen sorbents still faces a number of challenges. For instance, oxygen release from SF requires very low P_{O_2}, which occurs either under vacuum or with significant amount of purge steam.[26,37] Both would incur significant energy and cost penalties. Meanwhile, oxygen capacities of SF based sorbents still has room for improvement, especially at lower temperatures (<600°C).[37,38] These challenges can be overcome by improving the oxygen sorbents' kinetic and thermodynamic performances. To this end, many attempts to optimize doped SF sorbents have been made through a trial and error type of approach owing to the lack of fundamental understanding and absence of effective descriptors.

To improve the efficiency of materials screening and optimization, a number of high-throughput studies have been performed using first-principles calculations.[23,39] These studies have the potential to efficiently screen promising candidates. However, previous studies generally focused on screening material candidates by calculating and screening their thermodynamic parameters. They tend to

be computationally intensive because comprehensive calculations of detailed thermodynamic properties are required. A potentially more computationally efficient approach is to identify a physically meaningful descriptor for materials screening through the establishment of the relationship between the materials' redox properties and their electronic structures.

To explore suitable descriptors for oxygen sorbent performances in CLAS, and to gain a deeper understanding of the effects of dopants on perovskites, we performed density functional theory (DFT) calculations on a series of SF-based perovskites with various A- site and B- site dopants (A= Ca, Ba, K, La, Y, B= Co, Cu, Mn, Ni). We initially studied Y and Cu doped SF and found that, compared to oxygen p-band center (ε_p), the net electronic charge (Δe) of oxygen anions showed a better correlation with the oxygen formation energy. The same conclusion was made in other doped SF systems. The finding was verified experimentally. Moreover, we determined that the lattice oxygen transport properties are closely related to the electronic structures and can be well described by both Δe and ε_p. The validity and efficiency of Δe make it a promising descriptor for oxygen sorbent performances and optimization.

2. COMPUTATIONAL AND EXPERIMENTAL DETAILS

2.1. Computational details. First-principles simulations were performed at the DFT level implemented by the Vienna ab initio Simulation package (VASP)[40] with the frozen-core all-electron projector augmented wave (PAW) model[41] and Perdew-Burke-Ernzerhof (PBE) functions.[42] We used PAW potentials with the following electronic configurations: Sr ($4s^2\ 4p^6\ 5s^2$), Fe ($3d^7\ 4S^1$), Ca ($3s^2\ 3p^6\ 4s^2$), Ba ($5s^2\ 5p^6\ 6s^2$), K ($3s^2\ 3p^6\ 4s^1$), La ($5s^2\ 5p^6\ 6s^2\ 5d^1$), Y ($4s^2\ 4p^6\ 4d^1\ 5s^2$), Co ($3d^8\ 4s^1$), Cu ($3d^{10}\ 4p^1$), Mn ($3d^6\ 4s^1$), and Ni ($3d^9\ 4s^1$) (see Supporting Information). A kinetic energy cutoff of 450 eV was used for the plane-wave expansion of the electronic wave function, and the convergence criterions of force and energy were set as 0.01 eV $Å^{-1}$ and 10^{-5} eV respectively. A Gaussian smearing of 0.1 eV was applied for optimizations. A k-point grid with a 4 × 4 × 4 Gamma-centered mesh for sampling the first Brillouin zone was chosen for SF-based 2 × 2 × 2 supercell, which contains 40 atoms. The strong on-site coulomb interaction on the d-orbital electrons on the transition metal sites were treated with the GGA+U approach.[43] We adopted U_{eff} = 4, 4, 3.4, 3.9, 6 eV for Fe, Cu, Co, Mn, Ni sites, which have been proven to give reasonable predictions of both geometric and electronic structures in previous works.[44,45] Charge distribution analysis was performed using the density-derived electrostatic and chemical (DDEC06) atomic population analysis method.[46] Using this method, the net electronic charge (Δe) can be easily obtained with a single-point electronic structure calculation. The climbing image nudged elastic band (CI-NEB) method was applied for transition sate optimization.[47]

The energy of O_2 is computed by $E(O_2) = E(O) - \Delta E_{binding}$ due to the well-known overbinding issue of the O_2 molecule within DFT,[48,49] where $E(O)$ represent the energy of O atom and $\Delta E_{binding}$ (-5.15 eV) is computed using the CBS methods[50,51] using Gaussian 16.[52] The periodic boundary conditions were applied to all the studied models. The magnetic ordering structure of pristine SF was firstly studied due to the existing initial magnetic moments of Fe ions. The ferromagnetic (FM) phase and three different types of antiferromagnetic (AFM) phases (A-, C- and G-AFM) (**Figure S1**) were considered under the collinear spin approximation for the 2 × 2 × 2 SF supercell. Results show that the lattice constants of these four magnetic phases are all slightly larger than the experimental value (3.85 Å),[53] and the FM phase is more stable than other magnetic phases (**Table S1**). These results are consistent with a previous report.[54] To make the simulations tractable, we thus used FM phase magnetic ordering for all the doped structures given that magnetic ordering has relatively small effects on the oxygen vacancy formation and migration.[55] To build the doped models, one out of every eight equivalent Sr (A-site) atoms was replaced by Ca, Ba, K, La, Y to build the A-site doped samples, while one out of eight equivalent Fe (B-site) atoms was replaced by Co, Cu, Mn, Ni to build the B-site doped samples. All doped species are named using the notation A/B.X, where A/B is the A or B site and X is the doped elements. For instance, A.Y and B.Cu refers to Y doped A-sited and Cu doped B-site in SF respectively.

The selection of vacancy sites is another important consideration in constructing the defect models. For our $Sr_8Fe_8O_{24}$, $Sr_7A_1Fe_8O_{24}$ and $Sr_8Fe_7B_1O_{24}$ periodic models, to mimic different δ (0.125, 0.25, 0.375 and 0.5), 1 to 4 vacancies should be created from 24 oxygen sites, corresponding to possibilities of $C_{24}^1 = 24$, $C_{24}^2 = 276$, $C_{24}^3 = 2024$ and $C_{24}^4 = 10626$ respectively. Even with symmetry and equivalent sites considered, the sample pool is still extremely large especially at high δ, making it very difficult to determine the global energy minimum of defective configurations. To make the sampling manageable, we assumed that the creation of the N^{th} vacancy will not change the positions of the pre-existing N-1 vacancies. Based on this assumption, we first removed one oxygen atom from the defective-free structure and got the most energetically favored configuration with δ = 0.125. Using this as the basis, we continued to create the next most energetically favored vacancy to get the model with δ = 0.25. Configurations with δ = 0.375 and 0.5 were subsequently created using the same approach. The vacancy sites were selected carefully by comparing the energies of all possible vacancy sites (**Figure S2a**). Since the machine-hours required to relax all the structures were expensive and did not provide justifiable improvements in accuracy, we only compared the energies of the unrelaxed models and the most stable ones were chosen for subsequent geometric and electronic optimizations. Taking the A.Ca as an example, there are 24 possible sites for the first oxygen vacancy selection in our $Sr_7Ca_1Fe_8O_{24}$ model. As shown in **Figure S2b**, we compared the static energies of these 24 $Sr_7Ca_1Fe_8O_{23}$ structures and then chose the most stable one as the model that contains

one vacancy by removing O11. Compared to previous studies which assume randomly distributed vacancy sites,[23] our study attempts to identify the more energetically favorable vacancies combinations. We note that although this approach may not generate the global minimum at high vacancy concentrations, it nevertheless provides a better representation of the vacancy formation energies compared to a randomized vacancy assumption.

2.2. Synthesis methods. A or B site doped perovskites (i.e., $Sr_{1-x}A_xFe_{1-y}B_yO_3$, A = K, Y, Ca, and Ba, B = Mn, Co, Ni, Cu) were synthesized using a modified Pechini method.[37,56] In a typical synthesis of $Sr_{1-x}A_xFe_{1-y}B_yO_3$, stoichiometric amounts of the nitrates were dissolved in 15 mL of deionized water. After that, citric acid was added at a 2.5:1 citric acid to precursor molar ratio of to the solution and stirred at 40°C for 30 min. Then, ethylene glycol was added at a ratio of 1.5:1, and the solution was heated at 80 °C for 3 h while being well stirred. The formed gel was then heated in a vacuum oven at 120 °C for 16 h. The dried sample was heated in a tube furnace under an air environment at 1000 °C for 8 h to remove the organic template and form the perovskite phase. Finally, the remaining sample was crushed and sieved to a particle size between 150 μm and 250 μm.

2.3. TGA Experiments. To determine equilibrium weight at various temperatures, the sorbent material was ramped to 700 °C at a ramp rate of 20 °C /min and held at the temperature for 5 minutes at a fixed oxygen partial pressure in a thermogravimetric analyzer (TGA, TA Instruments SDT Q650). The temperature was then stepped down to 450 °C in 50 °C increments. Once the temperature reached 450 °C the oxygen flowrates were changed, and the temperature was ramped back to 700 °C. Initial testing was conducted at high temperatures for kinetic considerations. Oxygen flowrates, which correspond to partial pressures of 20%, 5%, and 1% when total flowrate is 200 sccm, as chemical potential related to the logarithm of the oxygen partial pressure. These pressures were recorded on a Setnag oxygen analyzer and controlled using mass flow controllers (MFCs).

δ values in the $Sr_{1-x}A_xFe_{1-y}B_yO_{3-\delta}$ samples were calculated using $\delta = \frac{\Delta m M_w}{m M_O} + \delta(0)$ where Δm is the mass change during the redox reaction, M_w is the sample's molar mass, m is the initial mass, and M_o is the molecular weight of oxygen. δ(0) is the initial non-stoichiometry at ambient temperatures and oxygen partial pressures as prepared. It was determined by heating the sample to 1000 °C under an air environment. The gas was then switched to 20% H_2 balance Ar to fully decompose the sample and kept isothermal until weight stabilized to form reduced phases, in the case of $SrFeO_3$, they are SrO and Fe. δ(0)was then determined based on the decomposition reactions. For example, $SrFeO_{3-\delta}$ was determined using the equation $\delta(0) = \frac{2M_O - 3xM_O - x(M_{Sr}+M_{Fe})}{(1-x)M_O}$, where x is $\frac{W_i - W_f}{W_i}$ where W_i is the initial weight and $W_f$is the weight final, indicating that x is the total weight loss percentage and M_O, M_{Sr}, M_{Fe} is the molecular weight of oxygen, strontium and iron respectively.

3. RESULTS AND DISCUSSION

3.1. CLAS and DFT based Descriptors for Oxygen Sorbent Performance. Figure 1 illustrates the operating mode for CLAS and the relationships between the intrinsic properties of an oxygen sorbent and its CLAS performance. As can be seen, CLAS operates in a two-step redox cycle, which reversibly absorbs and desorbs oxygen under oxygen partial pressure (P_{O_2}) and/or temperature swings. In the oxidization step (left), SF captures O_2 from the air and thus reduces its oxygen non-stoichiometry (δ). Subsequently, in the oxygen generation step (right), the sorbent releases oxygen at low P_{O_2} due to the reduction in oxygen chemical potential (μ_{O_2}) that shifts the chemical equilibrium, thereby achieving efficient separation of oxygen from the air. Given that the oxygen sorbent is at the center of the CLAS process, its redox performances, i.e. lattice oxygen storage capacity and release/uptake rates, are critical for the overall attractiveness of CLAS. Meanwhile, the unique oxygen nonstoichiometry in perovskite-based oxygen sorbents, e.g. SF, makes the process highly dynamic. Unlike conventional, monometallic redox pairs such as Mn_3O_4/MnO_2, the oxygen storage capacities of perovskite-based oxygen sorbents are affected by the operating windows, i.e. changes in operating temperatures and oxygen partial pressures in the redox steps can affect the variation in oxygen nonstoichiometry of the perovskite-based oxygen sorbents, and hence their oxygen capacities and redox kinetics. Moreover, perovskites have a high degree of tunability in terms of compositional, structural, and redox properties. Such complex relationships, in principle, can be correlated with DFT based descriptors such as: (a) oxygen vacancy formation energy, which describes the ease of oxygen release from a thermodynamic standpoint; and (b) energy barrier for oxygen vacancy migration, which, along with vacancy formation energy, describe the rates of oxygen release/uptake, given that a number of previous studies indicate that lattice oxygen conduction being the rate limiting step in chemical looping reactions.[15,57-59]

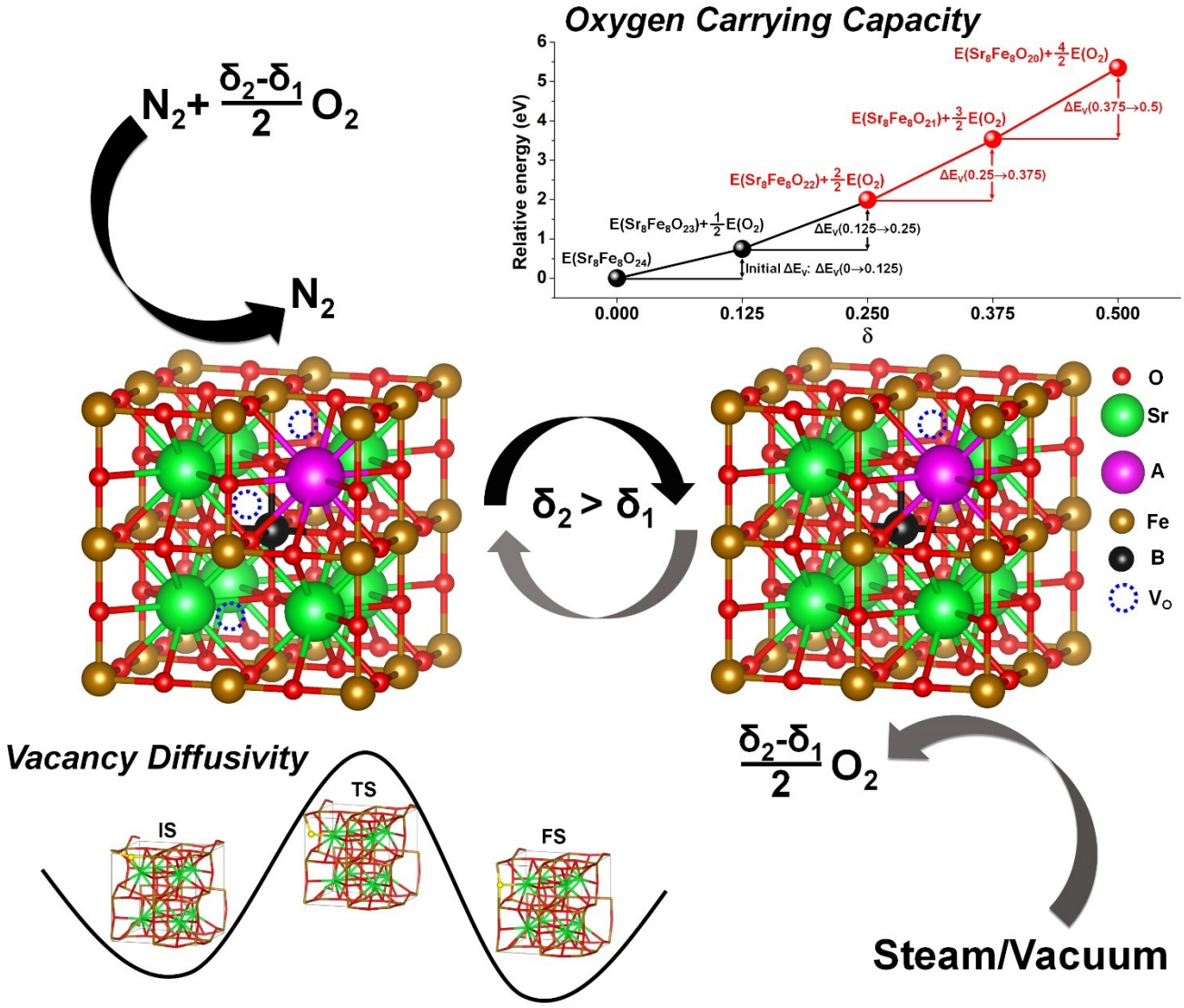

Figure 1. Illustration of the operating mode for CLAS and the relationships between the intrinsic properties of an oxygen sorbent and its CLAS performance. Lower (incremental) oxygen vacancy formation energy corresponds to higher (thermodynamic based) oxygen carrying capacity. Lower oxygen vacancy migration barrier, along with high vacancy concentration, leads to higher vacancy diffusivity.

Previous studies had some success using the initial vacancy formation energy from a perfect perovskite structure as a descriptor for oxygen sorbent performance.[14,60,61] However, the initial vacancy formation energy alone may not correlate well with the sorbent performance due to the following reasons: (1) under practical CLAS operating conditions, the sorbents rarely start from a defect-free state; (2) both vacancy concentration and vacancy formation energy would change with oxygen partial pressure swings in CLAS; (3) the initial vacancy formation energy does not provide information with respect to the rates for oxygen/vacancy migration, which is crucial to the oxygen transport properties. As illustrated in **Figure 1** (upper right corner), an optimal oxygen sorbent should demonstrate a suitable level of incremental vacancy formation energy (slope, which is determined by the μ_{O_2} change under the P_{O_2} swing) within a large span of vacancy concentration (δs, to ensure large oxygen capacity). In addition, low energy barriers for vacancy migration are desirable to ensure fast redox kinetics. Although these DFT based descriptors would be more comprehensive for oxygen sorbent design, they are significantly more computationally intensive than initial vacancy formation energy. In the following sections, the reliabilities of these descriptors are discussed first. This is followed with the exploration of more computationally efficient descriptors for oxygen sorbent design and optimization.

3.2 Δe as a Descriptor for Vacancy Formation Energy and Oxygen Storage Capacity. As discussed in the previous section, although the initial vacancy formation energies ($\Delta E_V(0\rightarrow0.125)$) of SF-based oxygen sorbents tend to correlate well with the initial oxygen release temperatures determined by temperature programmed reduction (TPR)

experiments (**Figure S3**),[56,62] they are not adequate to predict the overall sorbent performance parameters such as oxygen capacity (**Figure S4**). Rather, oxygen vacancy formation energy as a function of oxygen non-stoichiometry (δ) can provide a more comprehensive picture on both the feasibility of an oxygen sorbent and its oxygen storage capacity. To verify the effectiveness of this approach, the relative energy of a few SF-based oxygen sorbents at different oxygen vacancy levels were calculated. The slopes between adjacent vacancy levels were studied as they indicate the required incremental energy when an additional vacancy is created. Therefore, lower slopes would correspond to easier oxygen release. Given that the slope can be written as $\Delta E_V(\delta_1 \rightarrow \delta_2)/0.125$, the ΔE_V at different δ ranges holds the potential as an indicator for the feasibility of oxygen release as well as oxygen carrying capacity under specific temperature and P_{O_2} swings. To verify its reliability, we tried to connect this with the experimentally determined oxygen capacities. Here the A-site Y doped SF (A.Y) and B-site Cu doped SF (B.Cu) (**Figure 2a**) were chosen due to their significant inhibition and promotional effects to the oxygen capacity respectively (**Figure 2b**) based on previous experimental findings.[56] At low temperatures (450~500 ℃) and within a 1% - 20% P_{O_2} swing, B.Cu shows the largest oxygen capacity, while the performances of SF and A.Y are comparable. This experimental trend agrees well with their close $\Delta E_V(0.25 \rightarrow 0.375)$ in the left side of **Figure 2c** given that the experimental δ range is between 0.34 and 0.4 (**Figure S5a**). At higher temperatures (550~700 ℃), corresponding to the experimental δ range of ~0.38 to 0.48 (**Figure S5b**), the oxygen capacity of these three species follow a trend of A.Y < SF < B.Cu, indicating a ΔE_V trend of A.Y > SF > B.Cu. This is satisfactorily predicted from our calculations $\Delta E_V(0.375 \rightarrow 0.5)$ in **Figure 2c** (left panel). It is worth noting that while SF at low δ typically exhibits a cubic perovskite structure, with the increase of δ, the oxygen vacancies will undergo orderly rearrangements, forming brownmillerite structures (**Figure S6**).[37] To ensure accuracy for our calculations, we also calculated the vacancy formation energies of brownmillerite A.Y, SF and B.Cu, shown in the right panel of **Figure 2c**. As it can be seen, vacancy formation energies in the brownmillerite structured sorbents exhibited the same trend as that of perovskites. This indicates that cubic perovskite models can potentially be sufficient to correlate with the entire range of oxygen vacancies under typical CLAS operating conditions. The consistency between experimental results and DFT calculations confirms the feasibility of $\Delta E_V(\delta)$ as an indicator for the experimental oxygen capacity.

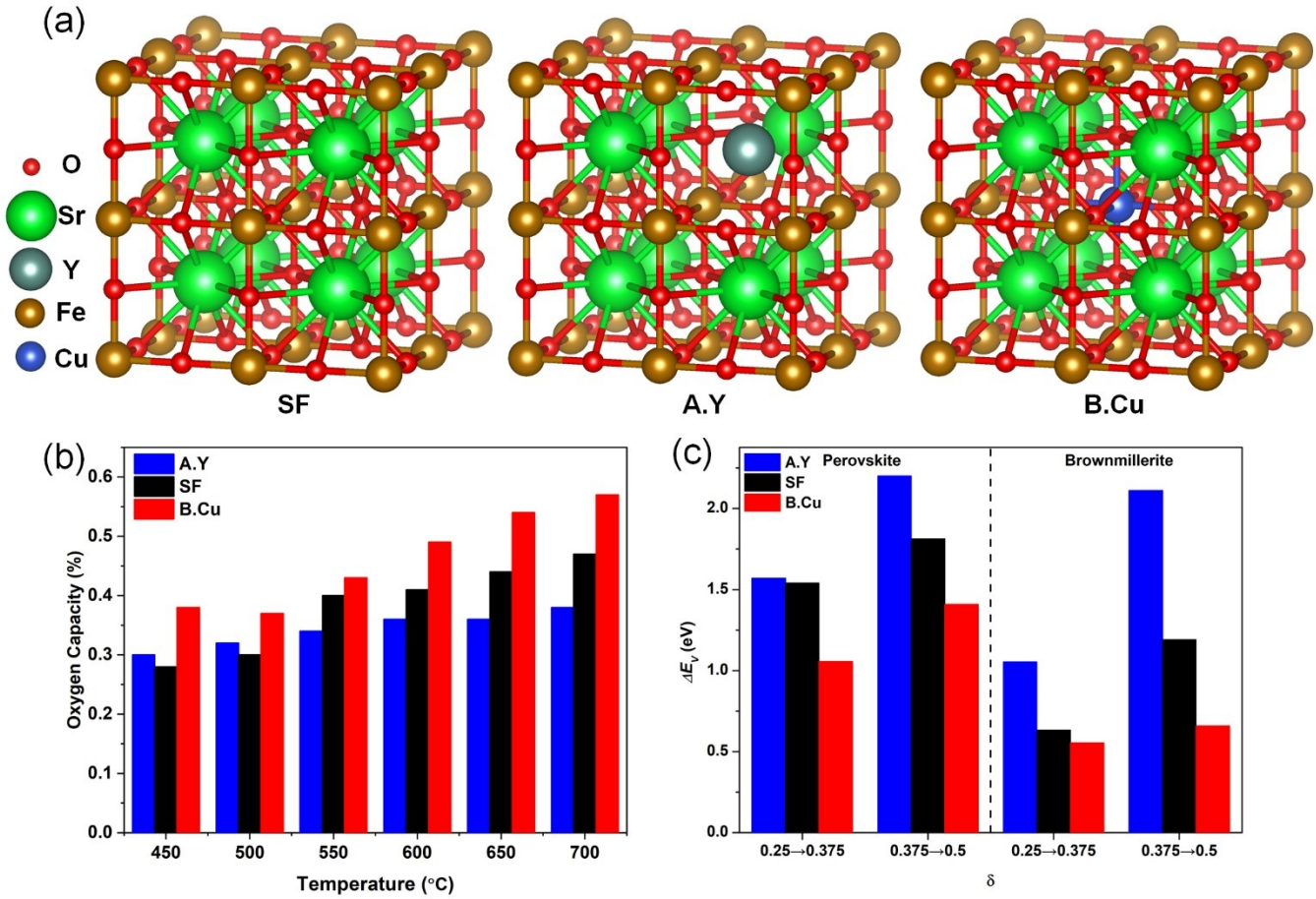

Figure 2. (a) Model structure of the $SrFeO_3$ (SF), A-site Y doped SF (A.Y) and B-site doped SF (B.Cu). (b) Experimental isothermal oxygen capacity for $SrFeO_3$, $Sr_{0.9}Y_{0.1}FeO_3$, and $SrFe_{0.9}Cu_{0.1}O_3$ when P_{O_2} is varied between 20% and 1%.[56] (c) Computed oxygen vacancy formation energies of A.Y, SF and B.Cu at different δ range from 0.25 to 0.5 based on perovskite (left) and brownmillerite (right) model.

The information gleaned above highlights the importance of ΔE_V as a function of δ in evaluating the performance of oxygen carriers. To determine the effect of dopants on oxygen sorbent performances, both geometric and electronic structural variations were studied. Firstly, we examined the impacts of structural variations on ΔE_V. As listed in **Table S2**, the lattice constants of Y and Cu doped samples slightly shrink from 7.757 Å to 7.745 and 7.753 Å respectively due to their relatively smaller ionic radii, whereas the changes in lattice angles are negligible. Although the lattice distortion induced by Y and Cu doping are similar, their impacts on ΔE_V are very different. This indicates that lattice distortions alone cannot explain the changes of ΔE_V. Meanwhile, the impact of changes in unit cell volumes on ΔE_V were also studied, as plotted in **Figure S7**. Although the trend shows a somewhat positive relation, their Pearson's correlation coefficient (PCC), which is a factor to estimate the correlation between two sets of parameters, is relatively low (0.79). This indicates that the volume change caused by doping also cannot correlate well with ΔE_V.

Besides structural parameters, dopants can alter the electronic structure of the perovskite which in turn changes ΔE_V. Therefore, Bader charge analysis was applied to estimate the charge redistribution in A.Y and B.Cu compared with pristine SF. The net electronic charge Δe was used to quantify the point charge of each ion, which is defined as the difference between the number of electrons on the ion N(ion) and a free-standing, neutral atom N(atom): $\Delta e = N(ion) - N(atom)$. It is apparent from **Figure 3a** that the doped Y cation donates more electrons (~1.90 e^-) compared to the initial Sr at the same site (~1.47 e^-) throughout the δ range investigated. Meanwhile, Cu donates less electrons (~1.27 e^- when δ=0 and as low as ~0.16 e^- when δ=0.5) compared to Fe at the same site in SF (~1.61 e^- when δ=0 and as low as ~1.25 e^- when δ=0.5). This indicates that Y doping is of the n-type while Cu doping is of the p-type. Consequently, oxygen anions would get more electrons from the Y dopant and less electrons from Cu, when compared to the SF parent structure, as depicted in **Figure 3b**. Note that since oxygen vacancy formation would cause an n-type doping effect,[63] more vacancies (larger δ) can induce more electrons accumulating on oxygen sites. However, at the same δ level, Δe on oxygen anions always follow a trend of A.Y > SF > B.Cu. It should also be noted that the atomic charge computed by commonly used methods such as DDEC06 provides a relative, as opposed to an absolute measure of the real atomic charge, which can be rationalized by the charge-self regulation mechanism.[64] Therefore, the presented atomic charges, albeit appearing to be small, are sufficiently reliable to show the trend that Y dopant injects electrons while Cu dopant injects holes to O sites. The spatial distribution of extra electrons and holes induced by Y and Cu doping are visually displayed in **Figure 3c** and **3d**, showing delocalized distributions. This also demonstrates that the variation of charge density and distribution on oxygen sites is caused by different types of cation substitutions.

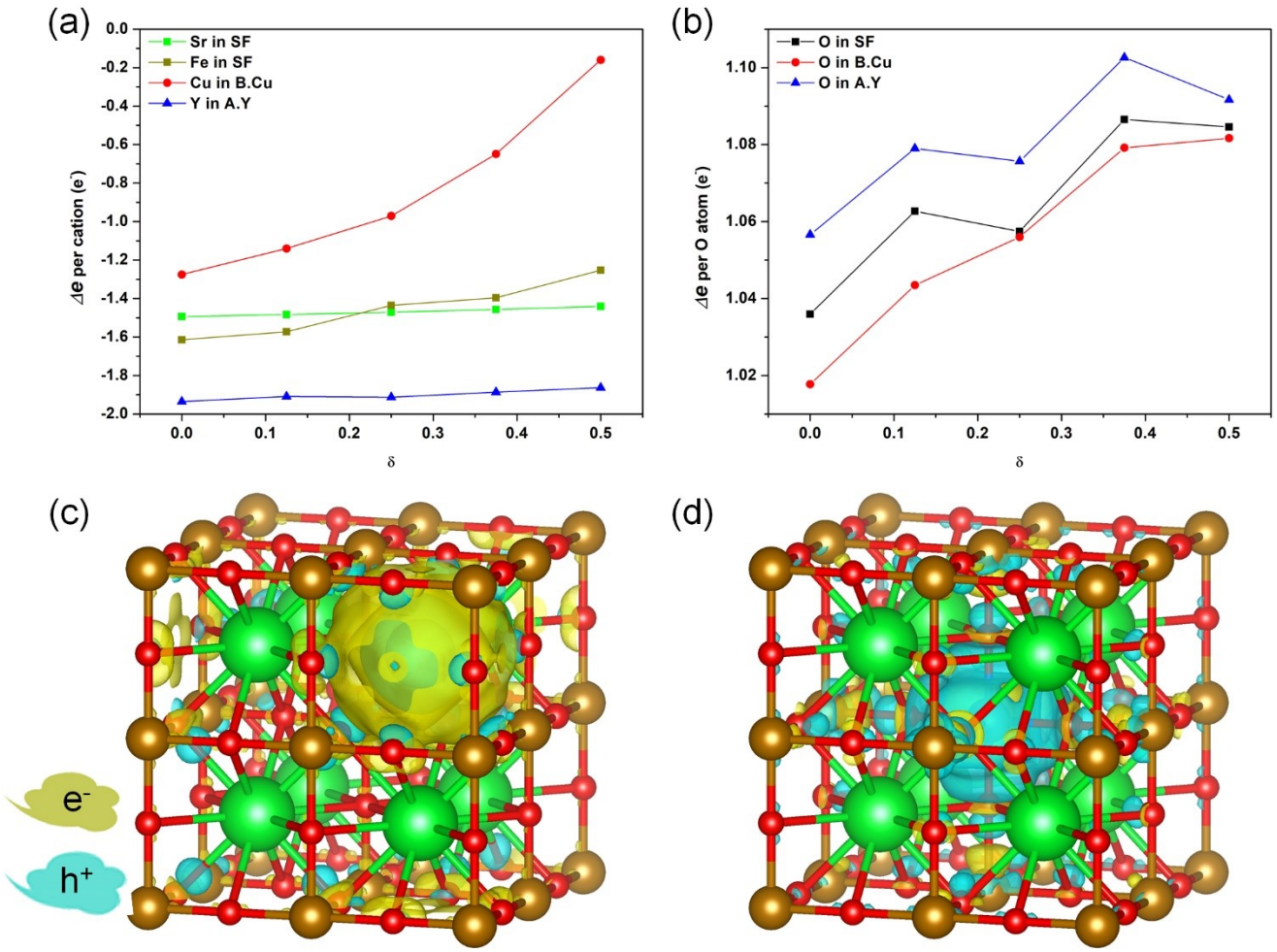

Figure 3. (a) Δe of Y in A.Y, the same site of Sr in SF, Cu in B.Cu and the same site of Fe in SF. (b) Δe per Oxygen atom in A.Y, SF and B.Cu. Differential charge density shows the accumulation of electrons (olive color) and holes (cyan color) after (c) A-site Y and (d) B-site Cu doping.

It is noted that Δe of lattice oxygen correlates well with ΔE_V, as shown in **Figure 4a**. The positive correlation and linear relationship indicate that the fewer electrons accepted by the lattice oxygen, the lower the ΔE_V. The PCC between Δe and ΔE_V is as high as 0.95, suggesting a very strong correlation. For comparison and inspired by the p-band theory,[65] which recently has been experimentally verified in describing the strength of metal-oxygen bonding,[66] we also plotted the relationship between p-band center (ε_p) and ΔE_V. Here ε_p is defined as

$$\varepsilon_p = \frac{\int E \cdot D(E - E_F) dE}{\int D(E - E_F) dE}$$

where D(E) denotes the projected density of states (PDOS) (**Figure S8**) of the O p-band and E_F is the fermi level energy. As shown in **Figure 4b**, although ε_p also correlates with ΔE_V, its PCC (0.85) is much lower than that of Δe (0.95). This indicates that Δe can more accurately describe ΔE_V. In addition, Δe is found to negatively correlate with ε_p (**Figure 4c**). Such a relationship is illustrated in **Figure 4d** using the p-band model. As it can be seen, different charge injections (p- or n-type doping) affect the occupation of electronic states. For an n-type doping (e.g. Y doping), the injected electrons occupy the empty metal 3d orbits and thus up-shift the Fermi level, moving the Fermi level away from the ε_p. A more negative ε_p means that the average energy of electrons in the O 2p orbitals is farther away from the frontier metal 3d orbitals, resulting in a less active oxygen sorbent (larger ΔE_V). In contrast, for a p-type doping (e.g. Cu doping), the injected holes would lower the Fermi level and thus making it closer to the ε_p. In the latter case, the hybridization of O 2p and transition metal 3d orbitals is enhanced, and consequently, the charge transfer gap between O 2p and metal 3d orbitals would be narrower, resulting in enhanced lattice oxygen activity.

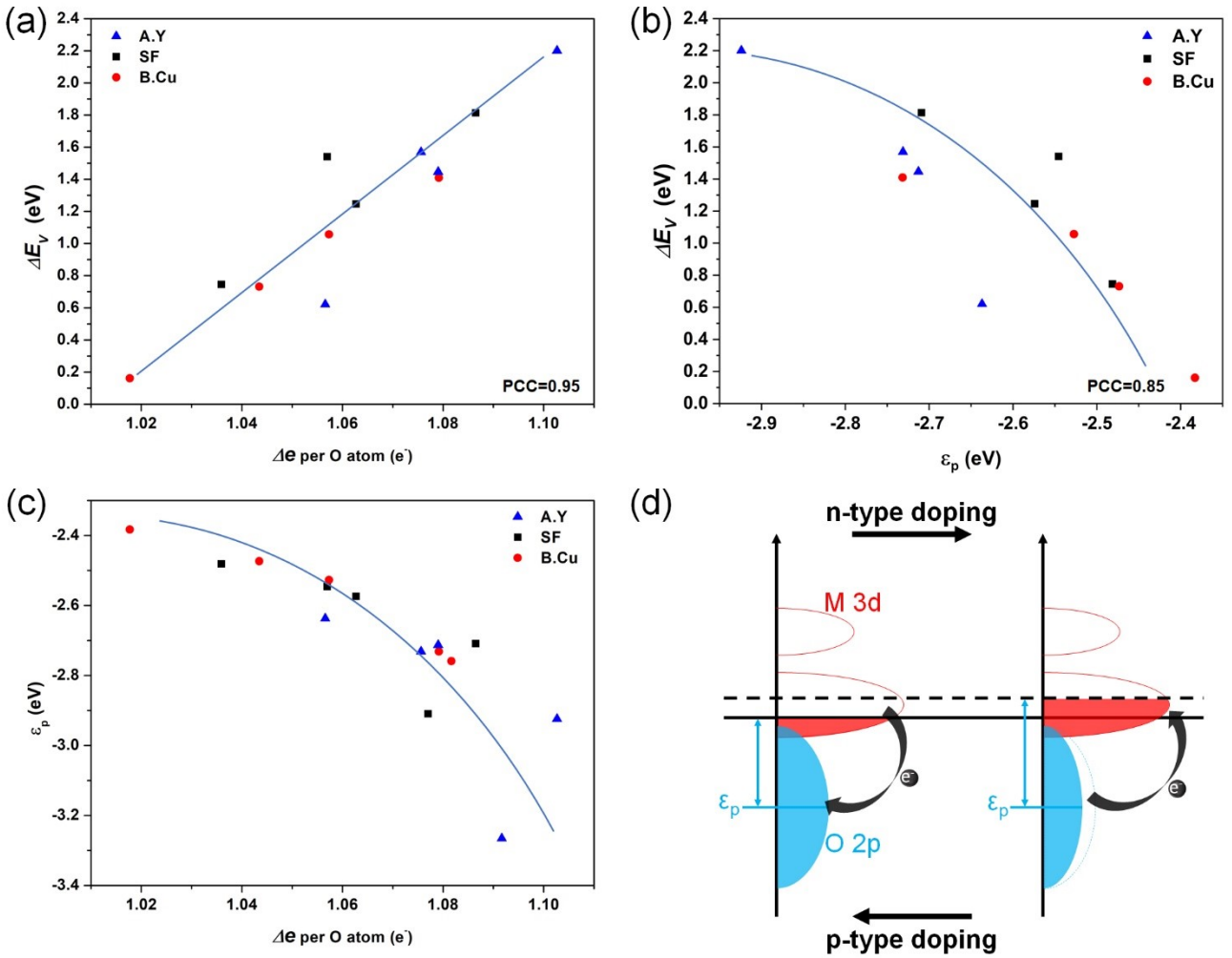

Figure 4. (a) Linear relationship between ΔE_V and Δe per O atom in A.Y, SF and B.Cu at different δs. (b) Correlation between ΔE_V and ε_p in A.Y, SF and B.Cu at different δs. (c) Correlation between Δe per O atom and ε_p in A.Y, SF, B.Cu at different δs. (d) Schematic illustration of SF-based perovskite density of states, showing the impact of n-type and p-type doping on the orbital occupation, Fermi level and ε_p.

To examine the applicability of Δe as an indicator for ΔE_V in a broader set of materials, the Δe dependence of ΔE_V in a series of doped samples including A.La, A.Ba, A.K, B.Co, B.Mn and B.Ni was investigated. Similar to the trend in SF, A.Y and B.Cu, Δe per oxygen atom for other doped species also follows a linear relationship with ΔE_V with a high PCC of 0.92 (**Figure 5a**). To compare, ε_p, which is negatively correlated with ΔE_V, has a lower PCC of 0.76 (**Figure 5b**). As expected, a negative correlation between Δe and ε_p is found (**Figure 5c**). Given the much higher PCC for Δe than ε_p, Δe is deemed to be a more effective descriptor for the vacancy formation energy, and hence redox thermodynamic properties of perovskite-based oxygen sorbents. To further determine whether Δe can accurately predict ΔE_V, the Random forests (RF) algorithm[67] implemented in the Scikit-learn Python library,[68] a supervised learning algorithm containing a forest of decision trees, was applied to analyze the existing data. ΔE_V was chosen as the target, and Δe and ε_p were used as features as shown in **Figure 5d**. The predicted ΔE_V values are obtained from weighted average of predictions of all the trees, exhibiting a very good correlation with the DFT computed values (PCC=0.90) and an acceptable the root-mean-square error (RMSE) of 0.28 eV compared to previous works.[69] Among the selected features, Δe acts as the dominant factor in determining the predictions with a high importance of 90%. To further verify its effectiveness, the RF model was retrained using Δe as the only descriptor. As shown in **Figure S9**, the prediction performance was remarkably good, with PCC=0.90 and RMSE=0.34 eV, which again demonstrates the efficacy of Δe in predicting ΔE_V.

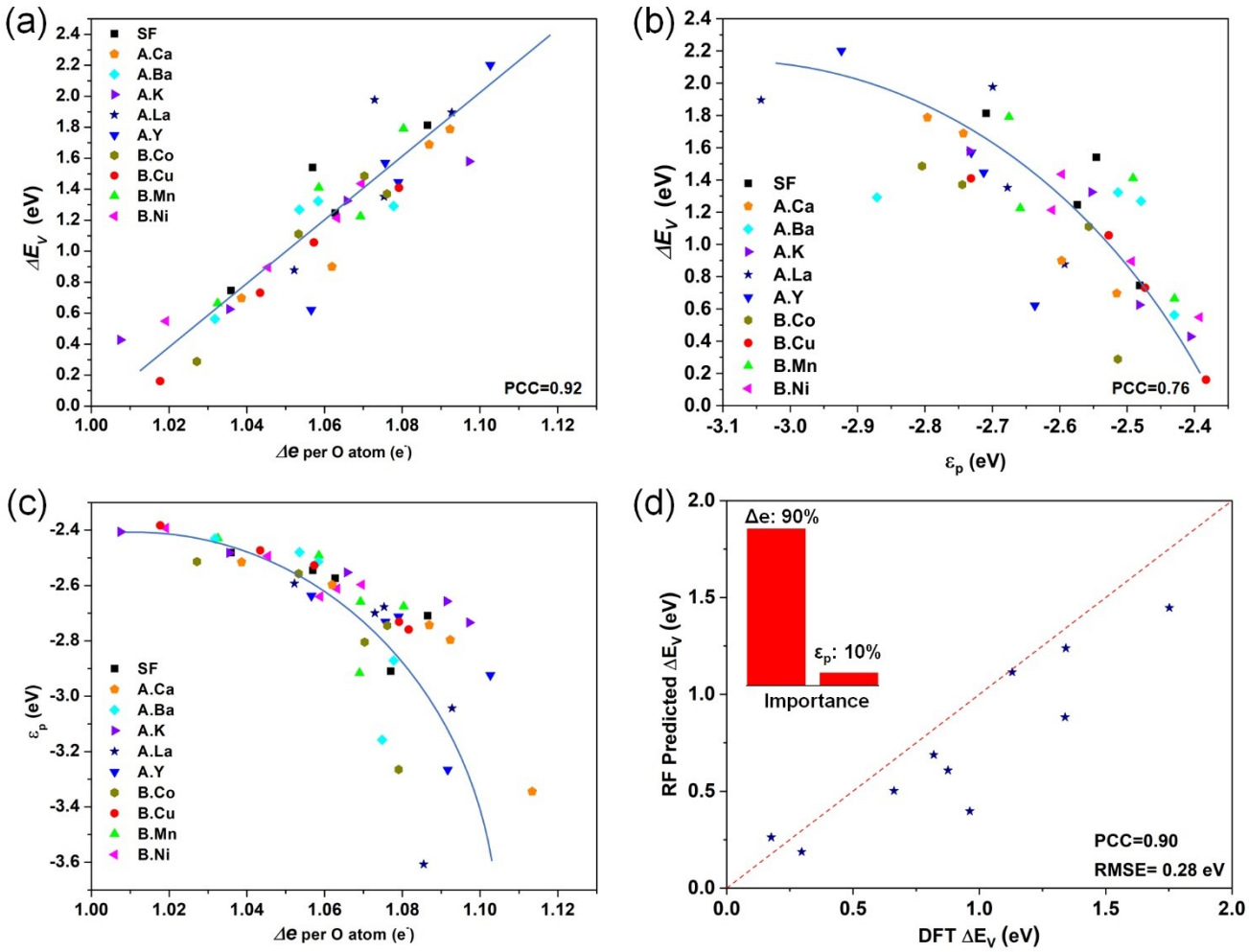

Figure 5. (a) Linear relationship between ΔE_V and Δe per O atom for different SF-based perovskites with δ = 0, 0.125, 0.25 and 0.375. (b) Correlation between ΔE_V and ε_p for different SF-based perovskites with δ = 0, 0.125, 0.25 and 0.375. (c) Correlation between Δe per O atom and ε_p for different SF-based perovskites with δ = 0, 0.125, 0.25 and 0.375. (d) Comparison of the RF predicted and DFT computed ΔE_V. Insert is the relative importance of Δe and ε_p. Here the importance of each feature is their percentage of contributions in making the final predictions. The red dashed line is intended to guide the eye.

Since the positive correlation between Δe and ΔE_V has been confirmed, Δe should also be correlate well with the experimental oxygen capacity and thus can also serve as a descriptor for oxygen capacity. To verify this point, the experimental oxygen capacities for various samples including SF, A.Ba, A.Y, B.Mn, B.Cu and etc. measured at 700 ℃ within 1% - 20% P_{O_2} swing[56] were compared with Δe and ΔE_V. Since the ranges of δ changes at such experimental conditions are roughly 0.3~0.5, the Δe (δ=0.375) and ΔE_V (δ:0.375→0.5) were selected for all the samples considered. The correlations based on perovskite models were plotted in **Figure 6a**. An inverse trend of experimental oxygen capacity vs. Δe (blue line) verifies the effectiveness of Δe (PCC = 0.80), which is only slightly worse than that of oxygen capacity vs. ΔE_V (PCC = 0.82). The difference may have originated from two aspects: (1) the calculations cover a slightly different δ range (0.375 – 0.5) compared to that in experiments (0.3 – 0.5); (2) cubic perovskite models were used in the calculation without considering a perovskite to brownmillerite transition. To address the latter aspect, calculations based on brownmillerite structures of these species were also performed (refer to **Figure S10-S17** and **Table S3** for more details). As plotted in **Figure 6b**, both Δe and ΔE_V are negatively correlated to the oxygen capacity, with higher PCCs than those obtained from perovskite models. Δe has a PCC (0.85) comparable to that for ΔE_V (0.87), showing its superior description capability. These findings verify the feasibility of using Δe as a descriptor for oxygen capacities of perovskite-based oxygen sorbents. It should be noted that we did not take the outlier sample B.Co into account when calculating the PCC, because the significant entropy increase caused by oxygen vacancies formation and sorbent decomposition cannot be described by simple ΔE_V or electronic structural calculations. In this case, we need to perform more time-consuming calculations to estimate the entropy and hence Gibbs free energy to get a better correspondence with the experimental oxygen capacity as shown in **Figure S18**. However, in most

cases, a simple electronic descriptor Δe is sufficient to predict the experimental oxygen capacity.

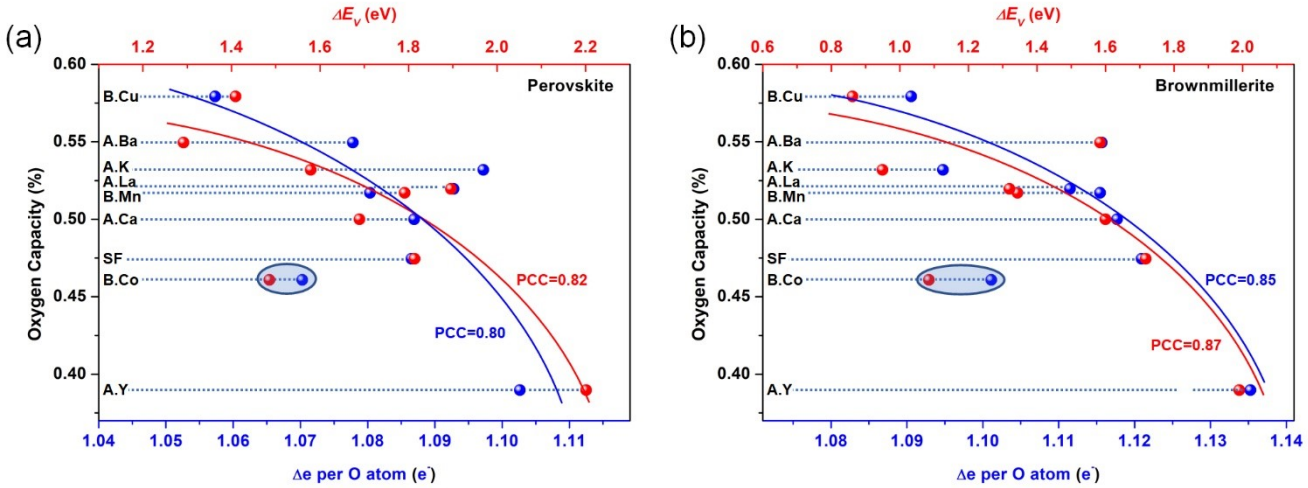

Figure 6. Experimental Oxygen capacity at 700 ℃ within 1% - 20% P_{O_2} swing as functions of ΔE_V and Δe for different SF-based (a) perovskite and (b) brownmillerite models.

3.3 Δe as a Descriptor for Oxygen Transport. The oxygen transport properties, which can be quantified by a combination of the vacancy formation energy and the vacancy migration barrier, is another important factor to determine the overall performance of an oxygen sorbent. However, computation of oxygen migration barriers is very computationally intensive, especially in large models because it involves very complex transition state (TS) searches. Finding an effective and easily accessible descriptor for the oxygen transport property is critical for understanding and improving the performances of oxygen sorbents. Since the TS search is very time-consuming, the undoped SF, A.Y and B.Cu perovskite structures were selected for further studies. To narrow down the possible oxygen migration pathways in each model, we only considered the migration of the oxygen atoms that are nearest to the vacancy sites, assuming that the migration of oxygen anions always follows the shortest route. In addition, unstable, symmetrical and equivalent pathways were ruled out. The remaining oxygen migration pathways of SF, A.Y and B.Cu with different δ (0.125, 0.25, 0.375 and 0.5) are displayed in **Figure S19-S22**, **Figure S23-S26** and **Figure S27-S30** respectively, with the most energetically favorable ones highlighted. The computed oxygen migration barriers of SF at δ=0.375 and 0.5 are 0.70 and 0.80 eV, which is consistent with the experimental value (0.83 eV at δ=0.4-0.5) obtained from the electrical conductivity relaxation (ECR) measurements (**Figure S31**). The barriers of each species are summarized in **Figure 7a**, showing the oxygen migration barriers roughly follow a trend of A.Y < SF < B.Cu. However, no obvious rule was found between δ and the migration barriers of each species. Before we continue to connect the migration barriers with electronic descriptors, it is worth noting that, as discussed earlier, the way we select vacancy sites does not guarantee the global minimum of the potential energy surface. Therefore, the energy of the final state (FS) after oxygen migration could be lower than the initial state (IS), as shown by the cases of A.Y (δ = 0.125, 0.25, 0.375), SF (δ = 0.375) and B.Cu (δ = 0.375) in **Figure 7a**. For these models, starting from FS, we continued to perform TS search to further explore their barriers (**Figure S32-S36**). It should also be noted that since our goal is to determine the relationship between barriers and electronic descriptors, the IS structures used here do not need to be the global energy minimums.

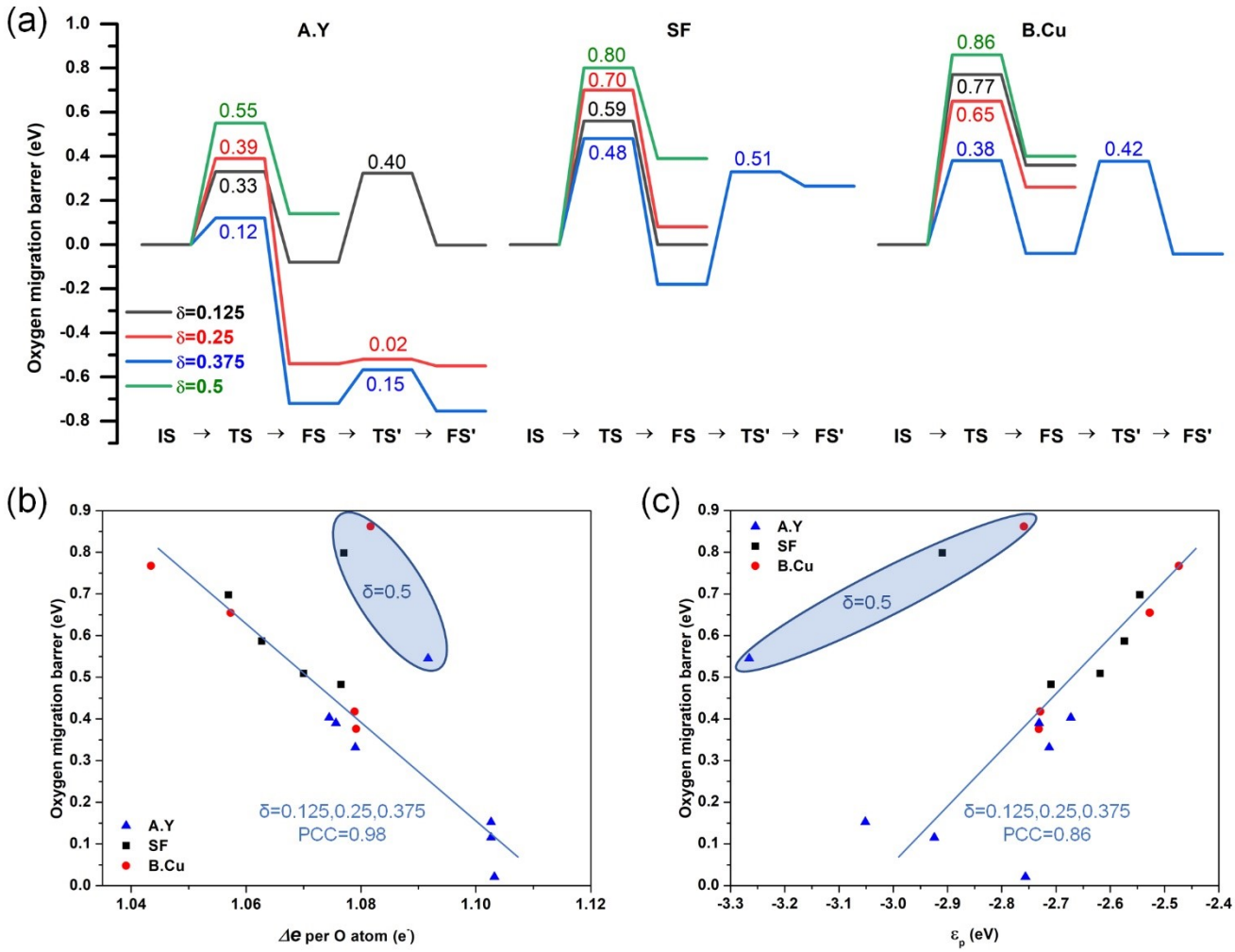

Figure 7. (a) Energy profiles of each elementary step of vacancy migration in A.Y, SF and B.Cu at different δ. All barriers are listed on corresponding energy level. IS, TS and FS represent initial, transition and final states. (b) Oxygen migration barrier as a function of Δe per O atom. (c) Oxygen migration barrier as a function of ε_p.

To correlate the migration barriers with electronic descriptors, we fit the barriers using Δe and ε_p. As shown in **Figure 7b**, an excellent linear relationship was observed between Δe and the barriers at low to intermediate δ levels (δ = 0.125, 0.25, or 0.375). At δ = 0.5, the vacancy formation energies appear to be outliers, this is likely to be due to phase transition from perovskite to brownmillerite. Since δ = 0.125 – 0.375 covers most of the practical operating range for oxygen sorbents in CLAS, this linear correlation is directly applicable for sorbent design and optimization. A satisfactory correlation was also identified for ε_p and the barriers for δ = 0.125 – 0.375 (**Figure 7c**). As can be seen, Δe exhibits near-perfect performance in describing the barriers (PCC = 0.98) at the operational δ ranges, demonstrating the superior performance of Δe in describing the barriers of oxygen migration. This opens a new and computationally efficient method for the study of oxygen carrier performances based on electronic descriptors.

4. CONCLUSIONS

Oxygen carrying capacity and redox kinetics represent the most important performance parameters for oxygen sorbents in chemical looping processes. In the current study, we report the net electronic charge (Δe) of oxygen anions as an effective and computationally efficient electronic descriptor for the design and optimization of $Sr_xA_{1-x}Fe_yB_{1-y}O_{3-\delta}$-based perovskite oxygen sorbents. It was first determined that vacancy formation energies of $Sr_xA_{1-x}Fe_yB_{1-y}O_{3-\delta}$, as a function of vacancy concentration, are closely correlated with their oxygen carrying capacities. However, detailed calculations of the vacancy formation energies for doped perovskites require a large number of test calculations (structural optimization calculations) to determine the favorable vacancy sites, which are highly computationally intensive. Compared to vacancy formation energy calculations, Δe can be directly calculated by a single-point calculation without trial-and-error, thereby reducing the computational intensity by two orders of magnitude. Meanwhile, an excellent correlation between Δe and vacancy formation energies was established. As such, Δe was shown to be highly efficient and accurate in predicting the experimentally derived oxygen carrying capacities for most

of the oxygen sorbents studied. Moreover, Δe was demonstrated to be an effective predictor for the energy barrier of vacancy migration and was superior to other electronic descriptors such as the p-band center (ε_p). Given that the vacancy migration barrier, together with vacancy concentration, determines the redox kinetics of an oxygen sorbent, Δe has an excellent potential to be an effective descriptor to assist the rational design and optimization of high-performance oxygen sorbents from both redox thermodynamics and kinetics standpoints. The new insights from this study can also be useful for investigating other oxygen-deficient mixed oxides in the context of redox applications.

ASSOCIATED CONTENT

Supporting Information.

The Supporting Information is available free of charge on the ACS Publication at DOI: 10.1021/acs.chemmater.??.

PAW pseudopotential used in this work, Figures of spin configurations, computed relative total energies of each spin configuration, model structure and relative energies of SF-based structures, reduction temperature as a function of ΔE_V, oxygen capacity as a function of ΔE_V, experimental δ swing ranges of A.Y and B.Cu, model structure of brownmillerite SF, computed lattice constants of SF, A.Y and B.Cu, ΔE_V as a function of lattice volume, computed PDOS, Comparison of RF predicted and DFT computed ΔE_V, model structures of brownmillerite A.Y, A.Ba, A.Ca, A.La, A.K, B.Mn, B.Cu, and B.Co, relative energies of oxygen addition in brownmillerite SF, A.Ba, A.Y, A.Ca, A.La, A.K, B.Mn, B.Cu and B.Co, experimental oxygen capacity as functions of ΔG, the oxygen migration pathway in SF, A.Y, and B.Cu at δ = 0,125, 0.25, 0.375, 0.5, correlation between the chemical diffusion coefficient and temperature.

AUTHOR INFORMATION

Corresponding Author

*fli5@ncsu.edu

Author Contributions

The manuscript was written through contributions of all authors.

Notes

The authors declare no competing financial interest.

ACKNOWLEDGMENT

This work was supported by the U.S. Department of Energy (Award No. FE0031521), the National Science Foundation (Grant No. CBET-1923468), and the North Carolina State University Kenan Institute for Engineering, Technology, and Science. We acknowledge the use of the Analytical Instrumentation Facility (AIF) at North Carolina State University, which is supported by the State of North Carolina and the National Science Foundation.

REFERENCES

(1) Bui, M.; Adjiman, C. S.; Bardow, A.; Anthony, E. J.; Boston, A.; Brown, S.; Fennell, P. S.; Fuss, S.; Galindo, A.; Hackett, L. A. Carbon capture and storage (CCS): the way forward. *Energy Environ. Sci.* **2018,** *11* (5), 1062-1176.

(2) Zhu, X.; Imtiaz, Q.; Donat, F.; Müller, C. R.; Li, F. Chemical looping beyond combustion–a perspective. *Energy Environ. Sci.* **2020,** *13* (3), 772-804.

(3) Zeng, L.; Cheng, Z.; Fan, J. A.; Fan, L.-S.; Gong, J. Metal oxide redox chemistry for chemical looping processes. *Nat. Rev. Chem.* **2018,** *2* (11), 349-364.

(4) Fan, L.-S.; Zeng, L.; Wang, W.; Luo, S. Chemical looping processes for CO 2 capture and carbonaceous fuel conversion–prospect and opportunity. *Energy Environ. Sci.* **2012,** *5* (6), 7254-7280.

(5) Lau, C. Y.; Dunstan, M. T.; Hu, W.; Grey, C. P.; Scott, S. A. Large scale in silico screening of materials for carbon capture through chemical looping. *Energy Environ. Sci.* **2017,** *10* (3), 818-831.

(6) Imtiaz, Q.; Hosseini, D.; Müller, C. R. Review of oxygen carriers for chemical looping with oxygen uncoupling (CLOU): thermodynamics, material development, and synthesis. *Energy Technol.* **2013,** *1* (11), 633-647.

(7) Bhavsar, S.; Veser, G. Chemical looping beyond combustion: production of synthesis gas via chemical looping partial oxidation of methane. *RSC Adv.* **2014,** *4* (88), 47254-47267.

(8) Liu, Y.; Qin, L.; Cheng, Z.; Goetze, J. W.; Kong, F.; Fan, J. A.; Fan, L. S. Near 100% CO selectivity in nanoscaled iron-based oxygen carriers for chemical looping methane partial oxidation. *Nat. Commun.* **2019**, 10, 5503.

(9) Haribal, V. P.; Neal, L. M.; Li, F. Oxidative dehydrogenation of ethane under a cyclic redox scheme–Process simulations and analysis. *Energy* **2017,** *119*, 1024-1035.

(10) Chen, S.; Zeng, L.; Mu, R.; Xiong, C.; Zhao, Z.-J.; Zhao, C.; Pei, C.; Peng, L.; Luo, J.; Fan, L.-S. Modulating Lattice Oxygen in Dual-Functional Mo–V–O Mixed Oxides for Chemical Looping Oxidative Dehydrogenation. *J. Am. Chem. Soc.* **2019,** *141* (47), 18653-18657.

(11) Gao, Y.; Wang, X.; Liu, J.; Huang, C.; Zhao, K.; Zhao, Z.; Wang, X.; Li, F. A molten carbonate shell modified perovskite redox catalyst for anaerobic oxidative dehydrogenation of ethane. *Sci. Adv.* **2020,** *6* (17), eaaz9339.

(12) Gao, Y.; Wang, S.; Hao, F.; Dai, Z.; Li, F. Zeolite-perovskite composites as effective redox catalysts for auto-thermal cracking of n-hexane. *ACS Sustainable Chem. Eng.* **2020**, 8 (38), 14268-14273.

(13) Hao, F.; Gao, Y.; Neal, L.; Dudek, R. B.; Li, W.; Chung, C.; Guan, B.; Liu, P.; Liu, X.; Li, F. Sodium tungstate-promoted CaMnO3 as an effective, phase-transition redox catalyst for redox oxidative cracking of cyclohexane. *J. Catal.* **2020,** *385*, 213-223.

(14) Mishra, A.; Li, T.; Li, F.; Santiso, E. E. Oxygen vacancy creation energy in Mn-containing perovskites: an effective indicator for chemical looping with oxygen uncoupling. *Chem. Mater.* **2019,** *31* (3), 689-698.

(15) Galinsky, N. L.; Huang, Y.; Shafiefarhood, A.; Li, F. Iron oxide with facilitated O2–transport for facile fuel oxidation and CO2 capture in a chemical looping scheme. *ACS Sustainable Chem. Eng.* **2013,** *1* (3), 364-373.

(16) Galinsky, N. L.; Shafiefarhood, A.; Chen, Y.; Neal, L.; Li, F. Effect of support on redox stability of iron oxide for chemical looping conversion of methane. *Appl. Catal. B* **2015,** *164*, 371-379.

(17) Arjmand, M.; Leion, H.; Mattisson, T.; Lyngfelt, A. Investigation of different manganese ores as oxygen carriers in chemical-looping combustion (CLC) for solid fuels. *Appl. Energy* **2014,** *113*, 1883-1894.

(18) Gu, H.; Shen, L.; Xiao, J.; Zhang, S.; Song, T. Chemical looping combustion of biomass/coal with natural iron ore as oxygen carrier in a continuous reactor. *Energy Fuels* **2011,** *25* (1), 446-455.

(19) Zhu, X.; Li, K.; Neal, L.; Li, F. Perovskites as geo-inspired oxygen storage materials for chemical looping and three-way catalysis: a perspective. *ACS Catal.* **2018,** *8* (9), 8213-8236.

(20) Hare, B. J.; Maiti, D.; Daza, Y. A.; Bhethanabotla, V. R.;

Kuhn, J. N. Enhanced CO2 conversion to CO by silica-supported perovskite oxides at low temperatures. *ACS Catal.* **2018,** *8* (4), 3021-3029.
(21) Sarshar, Z.; Kleitz, F.; Kaliaguine, S. Novel oxygen carriers for chemical looping combustion: La 1– x Ce x BO 3 (B= Co, Mn) perovskites synthesized by reactive grinding and nanocasting. *Energy Environ. Sci.* **2011,** *4* (10), 4258-4269.
(22) Bulfin, B.; Vieten, J.; Starr, D.; Azarpira, A.; Zachäus, C.; Hävecker, M.; Skorupska, K.; Schmücker, M.; Roeb, M.; Sattler, C. Redox chemistry of CaMnO 3 and Ca 0.8 Sr 0.2 MnO 3 oxygen storage perovskites. *J. Mater. Chem. A* **2017,** *5* (17), 7912-7919.
(23) Singstock, N. R.; Bartel, C. J.; Holder, A. M.; Musgrave, C. B. High-Throughput Analysis of Materials for Chemical Looping Processes. *Adv. Energy Mater.* **2020**, 2000685.
(24) Vieten, J.; Bulfin, B.; Huck, P.; Horton, M.; Guban, D.; Zhu, L.; Lu, Y.; Persson, K. A.; Roeb, M.; Sattler, C. Materials design of perovskite solid solutions for thermochemical applications. *Energy Environ. Sci.* **2019,** *12* (4), 1369-1384.
(25) Vieten, J.; Bulfin, B.; Call, F.; Lange, M.; Schmücker, M.; Francke, A.; Roeb, M.; Sattler, C. Perovskite oxides for application in thermochemical air separation and oxygen storage. *J. Mater. Chem. A* **2016,** *4* (35), 13652-13659.
(26) Luongo, G.; Donat, F.; Müller, C. R. Structural and thermodynamic study of Ca A-or Co B-site substituted SrFeO 3– δ perovskites for low temperature chemical looping applications. *PCCP* **2020,** *22* (17), 9272-9282.
(27) Galinsky, N.; Sendi, M.; Bowers, L.; Li, F. CaMn1–xBxO3– δ (B= Al, V, Fe, Co, and Ni) perovskite based oxygen carriers for chemical looping with oxygen uncoupling (CLOU). *Appl. Energy* **2016,** *174*, 80-87.
(28) Zheng, Q.; Lail, M.; Zhou, S.; Chung, C. C. CaCoxZr1–xO3– δ Perovskites as Oxygen-Selective Sorbents for Air Separation. *ChemSusChem* **2019,** *12* (12), 2598-2604.
(29) Jiang, Y.; Shen, Q.; Li, S.; Yang, G.; Huang, N. B-site cobalt-doped perovskite oxide BaNiO 3 oxygen sorbents for performance improvement of oxygen enriched gas production. *New J. Chem.* **2020,** *44* (15), 6003-6009.
(30) He, Y.; Zhu, X.; Li, Q.; Yang, W. Perovskite oxide absorbents for oxygen separation. *AlChE J.* **2009,** 55 (12), 3125-3133.
(31) Sihar, A. S.; Alias, N. H.; Shahruddin, M. Z.; Hassan, S. S. A. S.; Him, N. R. N.; Othman, N. H. Sol-gel-derived perovskite-based sorbents for high-temperature air separation. *J. Sol-Gel Sci. Technol.* **2019,** *89* (3), 776-784.
(32) Hao, P.; Shi, Y.; Li, S.; Liang, S. Oxygen sorption/desorption kinetics of SrCo 0.8 Fe 0.2 O 3– δ perovskite adsorbent for high temperature air separation. *Adsorption* **2018,** *24* (1), 65-71.
(33) Bulfin, B.; Lapp, J.; Richter, S.; Guban, D.; Vieten, J.; Brendelberger, S.; Roeb, M.; Sattler, C. Air separation and selective oxygen pumping via temperature and pressure swing oxygen adsorption using a redox cycle of SrFeO3 perovskite. *Chem. Eng. Sci.* **2019,** *203*, 68-75.
(34) Taylor, D. D.; Schreiber, N. J.; Levitas, B. D.; Xu, W.; Whitfield, P. S.; Rodriguez, E. E. Oxygen Storage Properties of La1–x Sr x FeO3– δ for Chemical-Looping Reactions—An In Situ Neutron and Synchrotron X-ray Study. *Chem. Mater.* **2016,** *28* (11), 3951-3960.
(35) Miura, N.; Ikeda, H.; Tsuchida, A. Sr1–x Ca x FeO3-δ as a New Oxygen Sorbent for the High-Temperature Pressure-Swing Adsorption Process. *Ind. Eng. Chem. Res.* **2016,** 55 (11), 3091-3096.
(36) Vieten, J.; Bulfin, B.; Senholdt, M.; Roeb, M.; Sattler, C.; Schmücker, M. Redox thermodynamics and phase composition in the system SrFeO3– δ—SrMnO3– δ. *Solid State Ionics* **2017,** *308*, 149-155.
(37) Dou, J.; Krzystowczyk, E.; Wang, X.; Robbins, T.; Ma, L.; Liu, X.; Li, F. A-and B-site Codoped SrFeO3 Oxygen Sorbents for Enhanced Chemical Looping Air Separation. *ChemSusChem* **2020,** *13* (2), 385-393.
(38) Ikeda, H.; Nikata, S.; Hirakawa, E.; Tsuchida, A.; Miura, N. Oxygen sorption/desorption behavior and crystal structural change for SrFeO3– δ. *Chem. Eng. Sci.* **2016,** *147*, 166-172.
(39) Emery, A. A.; Saal, J. E.; Kirklin, S.; Hegde, V. I.; Wolverton, C. High-throughput computational screening of perovskites for thermochemical water splitting applications. *Chem. Mater.* **2016,** *28* (16), 5621-5634.
(40) Kresse, G.; Furthmüller, J. Efficiency of ab-initio total energy calculations for metals and semiconductors using a plane-wave basis set. *Comput. Mater. Sci.* **1996,** *6* (1), 15-50.
(41) Blöchl, P. E. Projector augmented-wave method. *Phys. Rev. B* **1994,** *50* (24), 17953.
(42) Perdew, J. P.; Burke, K.; Ernzerhof, M. Generalized gradient approximation made simple. *Phys. Rev. Lett.* **1996,** *77* (18), 3865.
(43) Anisimov, V. I.; Zaanen, J.; Andersen, O. K. Band theory and Mott insulators: Hubbard U instead of Stoner I. *Phys. Rev. B* **1991,** *44* (3), 943.
(44) Jain, A.; Hautier, G.; Moore, C. J.; Ong, S. P.; Fischer, C. C.; Mueller, T.; Persson, K. A.; Ceder, G. A high-throughput infrastructure for density functional theory calculations. *Comput. Mater. Sci.* **2011,** *50* (8), 2295-2310.
(45) Hautier, G.; Ong, S. P.; Jain, A.; Moore, C. J.; Ceder, G. Accuracy of density functional theory in predicting formation energies of ternary oxides from binary oxides and its implication on phase stability. *Phys. Rev. B* **2012,** *85* (15), 155208.
(46) Manz, T. A.; Limas, N. G. Introducing DDEC6 atomic population analysis: part 1. Charge partitioning theory and methodology. *RSC Adv.* **2016,** *6* (53), 47771-47801.
(47) Henkelman, G.; Uberuaga, B. P.; Jónsson, H. A climbing image nudged elastic band method for finding saddle points and minimum energy paths. *J. Chem. Phys.* **2000,** *113* (22), 9901-9904.
(48) Kurth, S.; Perdew, J. P.; Blaha, P. Molecular and solid-state tests of density functional approximations: LSD, GGAs, and meta-GGAs. *Int. J. Quantum Chem* **1999,** *75* (4-5), 889-909.
(49) Wang, L.; Maxisch, T.; Ceder, G. Oxidation energies of transition metal oxides within the GGA+ U framework. *Phys. Rev. B* **2006,** *73* (19), 195107.
(50) Montgomery Jr, J. A.; Frisch, M. J.; Ochterski, J. W.; Petersson, G. A. A complete basis set model chemistry. VI. Use of density functional geometries and frequencies. *J. Chem. Phys.* **1999,** *110* (6), 2822-2827.
(51) Montgomery Jr, J. A.; Frisch, M. J.; Ochterski, J. W.; Petersson, G. A. A complete basis set model chemistry. VII. Use of the minimum population localization method. *J. Chem. Phys.* **2000,** *112* (15), 6532-6542.
(52) Frisch, M. J.; Trucks, G. W.; Schlegel, H. B.; Scuseria, G. E.; Robb, M. A.; Cheeseman, J. R.; Scalmani, G.; Barone, V.; Petersson, G. A.; Nakatsuji, H. et al. *Gaussian 16*. Revision C. 01; Gaussian Inc., Wallingford, CT, USA. 2016.
(53) Demazeau, G. Stabilization of Highest-Oxidation States of Transition Metals and the Induced Electronic Phenomena in Oxidic Perovskite Structures. *Z. Anorg. Allg. Chem.* **2005,** *631* (2-3), 556-563.
(54) Shein, I.; Shein, K.; Kozhevnikov, V.; Ivanovskii, A. Band structure and the magnetic and elastic properties of SrFeO 3 and LaFeO 3 perovskites. *Phys. Solid State* **2005,** *47* (11), 2082-2088.
(55) Lee, Y.-L.; Kleis, J.; Rossmeisl, J.; Morgan, D. Ab initio energetics of La B O 3 (001)(B= Mn, Fe, Co, and Ni) for solid oxide fuel cell cathodes. *Phys. Rev. B* **2009,** *80* (22), 224101.
(56) Krzystowczyk, E.; Wang, X.; Dou, J.; Haribal, V.; Li, F. Substituted SrFeO 3 as robust oxygen sorbents for thermochemical air separation: correlating redox performance with compositional and structural properties. *Phys. Chem. Chem. Phys.* **2020,** *22* (16), 8924-8932.

(57) Neal, L. M.; Shafiefarhood, A.; Li, F. Dynamic methane partial oxidation using a Fe2O3@ Lao. 8Sro. 2FeO3-δ core–shell redox catalyst in the absence of gaseous oxygen. *ACS Catal.* **2014,** *4* (10), 3560-3569.
(58) Li, F.; Luo, S.; Sun, Z.; Bao, X.; Fan, L.-S. Role of metal oxide support in redox reactions of iron oxide for chemical looping applications: experiments and density functional theory calculations. *Energy Environ. Sci.* **2011,** *4* (9), 3661-3667.
(59) Li, F.; Sun, Z.; Luo, S.; Fan, L.-S. Ionic diffusion in the oxidation of iron—effect of support and its implications to chemical looping applications. *Energy Environ. Sci.* **2011,** *4* (3), 876-880.
(60) Maiti, D.; Daza, Y. A.; Yung, M. M.; Kuhn, J. N.; Bhethanabotla, V. R. Oxygen vacancy formation characteristics in the bulk and across different surface terminations of La (1– x) Sr x Fe (1– y) Co y O (3– δ) perovskite oxides for CO 2 conversion. *J. Mater. Chem. A* **2016,** *4* (14), 5137-5148.
(61) Haribal, V. P.; He, F.; Mishra, A.; Li, F. Iron-doped BaMnO3 for hybrid water splitting and syngas generation. *ChemSusChem* **2017,** *10* (17), 3402-3408.
(62) Hurst, N. W.; Gentry, S. J.; Jones, A.; McNicol, B. D. Temperature programmed reduction. *Catal. Rev. Sci. Eng.* **1982,** *24* (2), 233-309.
(63) Wang, X.; Wang, Z.; Zhang, G.; Jiang, J. Insight into electronic and structural reorganizations for defect-induced VO2 metal–insulator transition. *J. Phys. Chem. Lett.* **2017,** *8* (13), 3129-3132.
(64) Raebiger, H.; Lany, S.; Zunger, A. Charge self-regulation upon changing the oxidation state of transition metals in insulators. *Nature* **2008**, *453* (7196), 763-766.
(65) Lee, Y.-L.; Kleis, J.; Rossmeisl, J.; Shao-Horn, Y.; Morgan, D. Prediction of solid oxide fuel cell cathode activity with first-principles descriptors. *Energy Environ. Sci.* **2011,** *4* (10), 3966-3970.
(66) Jacobs, R.; Hwang, J.; Shao-Horn, Y.; Morgan, D. Assessing correlations of perovskite catalytic performance with electronic structure descriptors. *Chem. Mater.* **2019,** *31* (3), 785-797.
(67) Breiman, L. Random forests. *Mach. Learn.* **2001,** *45* (1), 5-32.
(68) Pedregosa, F.; Varoquaux, G.; Gramfort, A.; Michel, V.; Thirion, B.; Grisel, O.; Blondel, M.; Prettenhofer, P.; Weiss, R.; Dubourg, V. Scikit-learn: Machine learning in Python. *J. Mach. Learn. Res.* **2011,** *12*, 2825-2830.
(69) Panapitiya, G.; Avendaño-Franco, G.; Ren, P.; Wen, X.; Li, Y.; Lewis, J. P. Machine-learning prediction of CO adsorption in thiolated, Ag-alloyed Au nanoclusters. *J. Am. Chem. Soc.* **2018,** *140* (50), 17508-17514.

SYNOPSIS TOC